The Journal of Experimental Biology **198**, 283–294 (1995)
Printed in Great Britain © The Company of Biologists Limited 1995

QUANTITATIVE FLOW ANALYSIS AROUND AQUATIC ANIMALS USING LASER SHEET PARTICLE IMAGE VELOCIMETRY

EIZE J. STAMHUIS AND JOHN J. VIDELER
Department of Marine Biology, University of Groningen, The Netherlands

Accepted 10 October 1994

Summary

Two alternative particle image velocimetry (PIV) methods have been developed, applying laser light sheet illumination of particle-seeded flows around marine organisms. Successive video images, recorded perpendicular to a light sheet parallel to the main stream, were digitized and processed to map the flow velocity in two-dimensional planes. In particle tracking velocimetry (PTV), displacements of single particles in two subsequent images were determined semi-automatically, resulting in flow diagrams consisting of non-uniformly distributed velocity vectors. Application of grid-cell averaging resulted in flow field diagrams with uniform vector distribution. In sub-image correlation PIV (SCPIV), repetitive convolution filtering of small sub-areas of two subsequent images resulted in automatic determination of cross-correlation peaks, yielding flow field diagrams with regularly spaced velocity vectors. In both PTV and SCPIV, missing values, caused by incomplete particle displacement information in some areas of the images or due to rejection of some erroneous vectors by the vector validation procedure, were interpolated using a two-dimensional spline interpolation technique.

The resultant vector flow fields were used to study the spatial distribution of velocity, spatial acceleration, vorticity, strain and shear. These flow fields could also be used to test for flow in the third dimension by studying the divergence, and to detect the presence and location of vortices. The results offer detailed quantitative descriptions of the flow morphology and can be used to assess dissipated energy. The versatile character of the technique makes it applicable to a wide range of fluid mechanical subjects within biological research. So far it has been successfully applied to map the flow around swimming copepods, fish larvae and juvenile fish and the ventilation current of a tube-living shrimp.

Key words: flow analysis, PIV, particle image velocimetry, sheet illumination, vector flow field, swimming, pumping, flow velocity, velocity gradients.

Introduction

Qualitative information about flow phenomena around organisms in water or in air is easily obtained by visualization of the flow using dye or smoke. The resulting streamlines and moving fronts provide a good impression of the flow direction (Vogel, 1981; Merzkirch, 1974).

Time sequences of images of neutrally buoyant particles, suspended in the fluid, offer quantitative information about the velocity and direction of the flow (Gupta and Lilley, 1985; Adrian, 1991). Since it is difficult to record and analyze paths of particles accurately in three dimensions, flows can alternatively be studied by recording particle paths in two-dimensional planes parallel to the main stream, as long as the flow perpendicular to this plane is relatively small. Images of particles in one thin slice of the fluid can be obtained by using a limited focal depth of the camera or by applying a thin sheet of light to illuminate the particles in one plane only (Merzkirch, 1974). Sheet illumination techniques, in particular, provide powerful means of flow visualization and quantitative analysis of interiors of flows (Hesselink, 1988). Successive images of one plane in a particle-seeded flow allow derivation of the speed and direction of the flow in that plane from the displacements of the particles. The results can be presented as velocity vectors.

Accurate quantitative studies of flow phenomena require a vector density high enough to show details of the flow pattern and a uniform vector distribution. When velocity data are used to derive gradient parameters, the vectors should ideally be available in a regular grid (Imaichi and Ohmi, 1983; Hesselink, 1988).

The particles used for particle image velocimetry (PIV) should ideally be neutrally buoyant and small compared with the fine flow structures studied and should interfere neither with the fluid nor with the organism.

PIV-like techniques, using micro-algae as tracing particles, have been used to study flow patterns caused by sessile and pelagic suspension-feeding organisms, such as lophophorates (Strathmann, 1973), brachiopods (LaBarbera, 1981), echinoderm larvae (Strathmann, 1971), ciliates (Fenchel,

1980), sea urchin larvae (Gilmour, 1986), other ciliated larvae (Emlet, 1990), copepods (Koehl and Strickler, 1981; Paffenhöfer *et al.* 1982; Strickler, 1982, 1985; Marrasé *et al.* 1990; Yen *et al.* 1991; Fields and Yen, 1993) and bivalves (Jørgensen, 1982). Small plastic beads and other artificial particles have been used to trace the feeding currents of simuliid dipteran larvae (Craig and Chance, 1982), the flow around the comb plates of ctenophores (Barlow *et al.* 1993), the vela of bivalve veliger larvae (Gallager, 1993) and models of polyps (Sponaugle, 1991) and to study suction feeding in fish and fish larvae (van Leeuwen, 1984; Drost *et al.* 1988). Flow patterns in air caused by flying birds have been visualized and analyzed using neutrally buoyant helium bubbles (Spedding *et al.* 1984; Spedding, 1986, 1987*a*,*b*).

The studies on suction feeding in fish and on flight in birds are based on the application of stereoscopic imaging. This allowed derivation of particle displacements in three dimensions and in time, which were analyzed by processing two-dimensional transections of the three-dimensional data sets.

In most of the studies mentioned, particles were traced manually and processed to single point velocities. The velocity vectors obtained were commonly not uniformly distributed, resulting in flow field diagrams with gaps where data were lacking. This hampers interpretation of the diagrams and complicates further processing. In only a few cases (Barlow *et al.* 1993; Fields and Yen, 1993; Gallager, 1993) were the particle data processed to calculate two-dimensional velocity fields consisting of iso-velocity areas.

Methods for recording and processing of reliable velocity vector diagrams have recently been developed in fluid mechanics (e.g. Adrian, 1991; Lourenço, 1991; Willert and Gharib, 1991; Hinsch, 1993). The flow, seeded with appropriate particles, is illuminated with a thin light sheet, often parallel to the main stream, and particle images on at least two successive moments are recorded photographically or on video tape. The images are enhanced if necessary, and velocity information is extracted from the images by tracking single particles (low seeding density) or by finding auto- or cross-correlations between sub-images (interrogation areas) using direct or indirect (using Fast Fourier Transforms) convolution filtering. Finally, the vectors are arranged in a regular grid resulting in a two-dimensional velocity vector diagram of the flow field. Prior to interpolating gaps in the flow field diagrams, the vector data should be validated (Raffel *et al.* 1992). Interpolation is best done using a spline interpolation procedure (Spedding and Rignot, 1993). Finally, velocity gradient parameters can be derived.

The aim of this paper is to present methods of obtaining and exploiting two-dimensional PIV data of flows around living aquatic animals, resulting in diagrams showing uniformly distributed velocity vectors. The resultant vector flow fields are used to study the spatial distribution in two-dimensional planes (of three-dimensional flows) of velocity, spatial acceleration, vorticity, strain, shear and divergence of the flow, and to detect the presence and location of vortices. Detailed quantitative descriptions of the flow morphology can be used to calculate the dissipated mechanical energy.

Materials and methods

Image acquisition

Particles in one plane of a fluid flow were illuminated by a light sheet with adjustable thickness, using a red light krypton laser (Coherent Innova 70 K, λ=647 nm, P_{max}=1 W) equipped with a high-speed shutter (nmLASER LS500F with SC-1100D controller), a glassfibre delivery system (Newport Inc, F-LFI), and focusing and light sheet optics (Newport Inc.). The particles were imaged using a high-resolution video camera (i2s: IEC862BC) with a macro-zoom lens (Nikon), mounted normal to the light sheet. The camera was electronically shuttered to prevent motion blur. The video frames were recorded using a U-matic-SP professional video recorder (Sony, VO-9600P with RS-232-C interface), which offers access to each of the two separate fields of each video frame. To prevent video interlace blurring, single fields were used for analysis.

Image analysis

Coordinates of the particles were obtained from image analysis on the first fields of two successive video frames using a personal computer (486DX) equipped with a video digitizer (Imaging Technology Inc, VS-100-AT, resolution 768×512 square pixels) and image acquisition, processing and analysis software (Difa Measuring Systems, T.E.A. Image Manager v3.3). The images were enhanced by improving the signal-to-noise ratio by background equalization combined with contrast stretching.

Depending on the seeding density and maximum particle displacement (Hesselink, 1988), the images were analyzed by applying one of two alternative PIV techniques: particle tracking velocimetry (PTV) or sub-image correlation PIV (SCPIV). PTV was used when the water was seeded with low density and when the average particle displacements were relatively large, whereas SCPIV was applied when high seeding densities were allowed and the maximum particle displacement was of the order of a few times the particle diameter.

During analysis using PTV, the image was binarized by a threshold operation at a grey level just above the average grey value. This resulted in images containing only white dots, representing the particles, against a black noiseless background. The particles in the successive images were coloured differently and the images were superimposed. Subsequently, the positions of the particles were detected automatically within a cursor box, which was placed manually around each pair of corresponding particles. To assess accurate coordinates, the particles on the black background were subjected to an edge detection procedure followed by a centroiding technique, calculating the centre of gravity from the particle contour. The coordinates were stored in the

orthogonal frame of reference of the digitizer. Together with the coordinates, *x*- and *y*-scaling factors and the time step between the two video frames were stored.

When applying sub-image correlation (SCPIV) to the two successive, already enhanced, video frames, cross-correlation was performed between pairs of sub-images from both frames at the same location in each frame, using direct convolution filtering (Gonzales and Wintz, 1987). This yielded correlation peaks with an offset from the sub-image centre of the same magnitude as the average particle displacement in this sub-area of the flow field. The exact centre of the peak was found by edge detection followed by centroid location. This process was repeated with the next pair of sub-images, until the whole flow field had been scanned automatically according to a mesh grid. To extract as much particle displacement information from the frames as possible, neighbouring sub-images had a 50 % overlap (Hinsch, 1993). Weak peaks, e.g. those caused by pale particle images, were rejected to avoid pollution of the resulting data set. The coordinates of the sub-image centres and of the cross-correlation peaks of all pairs of sub-images were stored together with scaling factors and the time step in the same way as in PTV.

Data validation and flow field completion

From the results of PTV, the magnitude and direction of the velocity vectors were derived directly from the displacements of the particles in the *x*- and *y*-directions and the time step between the two successive frames. The origin of each vector was situated at the position of the particle in the first frame. Because of the non-uniform particle distribution, the resultant flow field had a non-uniform vector distribution. To obtain a vector flow field with uniformly distributed vectors, local high concentrations of original vectors were reduced by averaging magnitudes and directions, and gaps were filled by interpolation. This process was facilitated by applying a mesh grid, dividing the flow field into rows and columns of square cells. Usually, the number of cells was selected to be smaller than the number of original vectors. Each cell was assigned one resultant velocity vector, starting at the centre of the cell, by averaging all the vectors in the cell.

The data resulting from SCPIV were also translated to vectors, which were already uniformly distributed and arranged in a grid, as a result of the grid-structured interrogation process.

Before further processing was performed (e.g. interpolation or gradient parameter derivation), a validation procedure was applied to the resultant vectors to delete erroneous vectors from the PTV or SCPIV results. Erroneous vectors were caused by errors during the image analysis, e.g. when two points were mistakenly considered to be a corresponding pair (PTV) or because of distortion effects at image rims and in areas with low local seeding (SCPIV). The vector validation procedure compared the velocity components **u** (*x*-direction) and **v** (*y*-direction) of a vector in a two-dimensional Eulerian velocity field with $\mathbf{u}_{\text{mean}} \pm$ S.D. and $\mathbf{v}_{\text{mean}} \pm$ S.D. of its surrounding vectors in a window of 3×3 cells. Only cells containing a vector contributed to the mean and S.D. of a 3×3 window. Vectors were selected for rejection when their **u** or **v** value was outside the confidence regions:

$$(\mathbf{u}_{\text{mean}} - S \times F_{\mathbf{u}} \times \text{S.D.}) < \mathbf{u}_{x,y} < (\mathbf{u}_{\text{mean}} + S \times F_{\mathbf{u}} \times \text{S.D.}), \quad (1)$$

$$(\mathbf{v}_{\text{mean}} - S \times F_{\mathbf{v}} \times \text{S.D.}) < \mathbf{v}_{x,y} < (\mathbf{v}_{\text{mean}} + S \times F_{\mathbf{v}} \times \text{S.D.}), \quad (2)$$

in which S is a sensitivity factor, $F_{\mathbf{u}}$ and $F_{\mathbf{v}}$ are flow type factors and x,y denotes the position in the velocity field.

The flow type factors depend on the general type of flow and vary between 1 (unidirectional, no gradients) and 2 (chaotic turbulence). They are calculated from the average differences in **u** ($\overline{\Delta \mathbf{u}}$) and **v** ($\overline{\Delta \mathbf{v}}$) between all neighbouring vectors in the flow field and the average magnitude **V** of all velocity vectors:

$$\mathbf{u} \text{ flow type factor} = F_{\mathbf{u}} = 1 + \frac{\overline{\Delta \mathbf{u}}}{\overline{\mathbf{V}}}, \quad (3)$$

$$\mathbf{v} \text{ flow type factor} = F_{\mathbf{v}} = 1 + \frac{\overline{\Delta \mathbf{v}}}{\overline{\mathbf{V}}}. \quad (4)$$

The sensitivity factor S ($0.5 \leqslant S \leqslant 2$) is a multiplication factor by which the rejection probability can be adjusted or set to a certain statistical standard. When, for example, $(S * F_{\mathbf{u}})=2$, the confidence region becomes 95 % and the level of significance for rejection therefore becomes 0.05.

Depending on the flow type factors $F_{\mathbf{u}}$ and $F_{\mathbf{v}}$ and the sensitivity factor S, the rejection probability varies between 33 % and 1 %, assuming normal distribution of **u** and **v** around their means. In a laminar or large-scale turbulent flow, applying intermediate sensitivity, the procedure rejects vectors with **u** or **v** values outside a confidence region of approximately 95 %.

Empty cells in the flow fields from both PTV or SCPIV were provided with a new vector by interpolating **u** and **v** of the velocity vectors of neighbouring cells. The interpolation procedure performed was a two-dimensional spline curve fitting technique which was developed on the basis of open cubic natural spline curve fitting (Greville, 1969). This procedure produced smooth fits with minimal curvature without affecting the original points. Empty cells with neighbours in the *x*- as well as in the *y*-direction were provided with a new vector based on an average from *x*-interpolation and *y*-interpolation. New vectors for empty cells at the rims of the flow field with neighbours in only one direction were based on interpolation in that direction only; no extrapolations were made.

To account for the presence of obstacles (objects or organisms) in the flow field, the interpolation procedure was performed independently on either side of an obstacle. Boundary cells around obstacles were included in the procedure to prevent loss of flow information in the boundary layer. The resulting approximated flow fields show uniform regular vector distributions, offering a detailed impression of the velocity distribution in the flow.

Post-processing and data presentation

The resultant vector data arrays could easily be manipulated and used for further processing. Masking effects of a background flow due to fluid motion neither generated by, nor related to, the organism under study were compensated by subtracting the estimated background flow vector (derived from distant particle displacements) from the resultant vectors. This yielded flow fields showing only the effect of the organism.

Local flow patterns (e.g. vortices) could be emphasized by subtracting the average flow velocities in the *x*- and *y*-directions from all vectors.

Spatial changes in the magnitude of the flow velocity were analyzed by calculating two types of spatial accelerations: the non-directional spatial acceleration (a_N) and the spatial acceleration along the stream line (a_S).

The non-directional spatial acceleration a_N is the vector sum of the rates of change of the velocity components **u** and **v** in the *x*- and *y*-directions (=partial derivatives). It expresses changes in linear as well as angular acceleration and is therefore related to dissipated energy in cases of inertial flow. The formula used to compute a_N consists of a first part calculating the magnitude, which is multiplied by a second part setting the sign of a_N: plus for net acceleration and minus for net deceleration:

$$a_N = \sqrt{\left(\frac{\partial \mathbf{u}}{\partial x}\right)^2 + \left(\frac{\partial \mathbf{v}}{\partial y}\right)^2} \times \frac{\frac{\partial \mathbf{u}}{\partial x} + \frac{\partial \mathbf{v}}{\partial y}}{\left|\frac{\partial \mathbf{u}}{\partial x} + \frac{\partial \mathbf{v}}{\partial y}\right|}. \qquad (5)$$

The spatial acceleration along the stream line a_S gives an impression of the spatial acceleration of the fluid in the direction of the local stream line; the local stream line is supposed to be tangential to the local velocity as represented by the velocity vectors. a_S represents linear acceleration only and is calculated in a different way. In the 3×3 window surrounding a particular cell, the magnitude and direction of the central vector are compared with those of every single surrounding vector. In each comparison, a partial a_S is calculated from the difference in the velocity magnitudes **V** and the distance between the vectors with reference to the axis *r* in the direction of their average stream line. The final a_S for the central cell is averaged from the individual contributions from the surrounding cells, each of them weighted according to its position with reference to the central vector. This results in significant contributions of vectors in front of or behind the central vector ± approximately 45° (depending on the weighting). Velocity gradients perpendicular to the local stream line do not contribute to the local a_S.

The formula used to calculate the a_S for a central cell in a 3×3 window is:

$$a_S = \left\{\sum_{i=1}^{n}\left[\frac{\partial \mathbf{V}_i}{\partial r_i} \times |\cos^p(\beta_i)|\right]\right\} \times \left\{\sum_{i=1}^{n} |\cos^p(\beta_i)|\right\}^{-1}, \qquad (6)$$

where **V** is the magnitude of the velocity vector, *r* is the reference axis in the direction of the local average stream line, $\cos^p(\beta_i)$ is the weighting factor depending on angle β denoting the relative position of the *i*th vector with reference to the central vector, *p* sets the degree of tolerance ($1 \leqslant p \leqslant 4$) and subscript *i* denotes a surrounding vector ($1 \leqslant i \leqslant 8$).

The vector data were also used to calculate vorticity ω, strain rate *e*, shear rate *h* and divergence Θ. These parameters provide additional information about the steepness and the direction of gradients in the magnitude and direction of the fluid velocity (Lighthill, 1986; Okubo and Ebbesmeyer, 1976). They were calculated using the partial derivatives of the velocity components **u** and **v** to both *x* and *y*. The partial derivatives were obtained by numerical differentiation of **u** and **v** to both *x* and *y*, comparing the velocity vector of each cell with the vectors of surrounding cells in a window of 3×3 cells.

$$\text{Vorticity} = \omega = \frac{\partial \mathbf{v}}{\partial x} - \frac{\partial \mathbf{u}}{\partial y}, \qquad (7)$$

$$\text{Shear rate} = h = \frac{\partial \mathbf{v}}{\partial x} + \frac{\partial \mathbf{u}}{\partial y}, \qquad (8)$$

$$\text{Strain rate} = e = \frac{\partial \mathbf{u}}{\partial x} - \frac{\partial \mathbf{v}}{\partial y}, \qquad (9)$$

$$\text{Divergence} = \Theta = \frac{\partial \mathbf{u}}{\partial x} + \frac{\partial \mathbf{v}}{\partial y}. \qquad (10)$$

Vortices were emphasized in the velocity vector diagrams by subtracting the average velocities in the *x*- and *y*-directions. Although very illuminating, this did not result in reliable location of vortices, because the average velocities depend on several factors, e.g. the size ratio between flow phenomena studied and the recorded flow field. To detect and locate vortices independently of such external factors, the discriminant for complex eigenvalues *d* for a two-dimensional flow field was used (Vollmers *et al.* 1983). This discriminant becomes negative if the local gradient tensor (matrix presentation of the partial derivatives of the velocity components) does not have real eigenvalues, but only complex ones. This indicates a vortex with its centre at the location where *d* is most negative.

d may also be calculated from the partial derivatives of the local velocity components **u** and **v** to *x* and *y*:

$$d = \left(\frac{\partial \mathbf{u}}{\partial x} + \frac{\partial \mathbf{v}}{\partial y}\right)^2 - 4 \times \left[\left(\frac{\partial \mathbf{u}}{\partial x} \times \frac{\partial \mathbf{v}}{\partial y}\right) - \left(\frac{\partial \mathbf{u}}{\partial y} \times \frac{\partial \mathbf{v}}{\partial x}\right)\right]. \qquad (11)$$

The vector data were visualized using arrows starting at the middle of the cell (or sub-image) pointing in the direction of the local flow, as derived from the particle displacements, with a length proportional to their magnitude. The velocity magnitude, spatial acceleration rates, vorticity, shear, strain and divergence, as well as *d*, were visualized by applying colour coding to the grid of cells, using two series of five colours, bright colours for positive values and dark colours for

negative values, dividing each range from maximum to minimum into five equal intervals. This resulted in diagrams offering easy interpretation of the information.

All processing of particle displacement data, peak location data, the resulting vector data and the presentations of vector diagrams and colour-coded diagrams was carried out on a 486DX-based PC using a computer program (PIVChart v3.2) developed by the first author.

Error evaluation

The main sources of errors in the final vector flow fields are the method of location of particles or correlation peaks and the interpolation procedure (Imaichi and Ohmi, 1983; Agüi and Jiménez, 1987; Willert and Gharib, 1991; Spedding and Rignot, 1993).

To estimate the particle location error for the centroiding procedure in our method, many tests were performed on computer-generated particle pair patterns that were distributed at random over the pixel array. A range of combinations of particle pair positions, inter-particle distances, particle diameters and threshold grey levels were analyzed and processed to provide statistical data. From these, we were able to conclude that the accuracy in particle or peak location using the centroiding method depended very little on the threshold grey level. The results appeared to be 100 % repeatable for threshold levels around the average grey level of the image; only thresholding near the lowest or the highest values found in the image caused small deviations of the order of a few tenths of a pixel. This error could be avoided easily by choosing intermediate thresholding grey levels.

The accuracy of particle location also depended on the particle image diameter, expressed in pixels. In our tests, we found an almost constant S.D. in particle position measurements of 0.1 pixels for particle images with a diameter greater than 4 pixels. The S.D. increased exponentially to its maximum value of about 0.3 pixels for diameters between 4 and 2 pixels. This error must be multiplied by $\sqrt{2}$ to find the error for the PTV displacement measurements, consisting of two location measurements. However, the averaging of more than two single particle displacement vectors per cell reduces the error of the resulting vector. In SCPIV, the offset peak location measurements depend in the same way on peak diameter as particles do, resulting in an average displacement error between 0.1 and 0.3 pixels.

The way in which the velocity vectors are affected by the centroid location error depends strongly on the displacement of the particles. We found S.D. values in the final velocity vectors of 1–5 % for PTV and 0.1–2 % for SCPIV; both methods are therefore accurate enough to permit the derivation of velocity gradient parameters.

The errors in particle pairing (PTV) and in sub-image correlation (SCPIV) can be estimated from the data validation procedure, assuming a vector with a **u** or **v** value outside the 95 % confidence interval as erroneous. In PTV, between 2 and 20 vectors, with an average of 6, out of an average data set of 500 vectors were selected for rejection, resulting in a particle pairing error between 0.2 % and 4 %, on average about 1 %. In SCPIV, between 1 and 18 out of a data set of 800 vectors were selected for rejection, resulting in a maximum correlation error of about 2.5 %. Since all erroneous vectors selected by the validation procedure were removed from the data set, particle pairing or correlation errors were almost eliminated.

The grid cell averaging followed by interpolation as applied to PTV results sometimes introduced additional interpolation errors if the grid resolution was set too high. Because of the irregular distribution of the original PTV vectors, the grid had to be chosen arbitrarily. This was done in a repetitive comparison of original vectors, cell-averaged vectors and resultant flow field, until the most plausible solution with regard to the vectors surrounding gaps was found. We estimate the errors in interpolated vectors on average to be less than 5 %. The errors of interpolated vectors of SCPIV flow charts will be even less, because the data were already arranged in a grid, and very few missing values occurred.

Applications

The PIV methods described were applied to flow patterns produced by three different marine animals: (1) the feeding current of a tethered copepod, (2) the ventilation current of a tube-living thallassinid shrimp, and (3) the vortex street behind a swimming juvenile mullet. The flow produced by the copepod (1) and the mullet (3) were seeded densely and were analyzed applying SCPIV. The flow in the tube produced by the shrimp (2) showed steep gradients with locally relatively large particle displacements; therefore, this flow was not seeded very densely and was analyzed using PTV.

The feeding current of a tethered copepod

The feeding current of a tethered copepod (*Temora longicornis*, metasome length approximately 1 mm) was illuminated using a horizontal laser light sheet of 0.1 mm thickness. The water was seeded with nylon beads (TSI Inc., diameter approximately 4 μm), with the same density as sea water.

After processing of the video recordings and the resulting correlation peak data, the feeding current of the copepod was described in flow fields of uniformly distributed velocity vectors as well as colour plots of the gradient parameters, the velocity magnitude, the spatial acceleration parameters and the discriminant for complex eigenvalues. These diagrams showed acceleration of the converging water flow in front of the animal, increasing flow velocity and positive spatial acceleration parameters (a_N and a_S), with little deceleration of the flow occurring behind the animal and decreasing velocity and small negative values for the spatial acceleration parameters (a_N and a_S). Relatively large vortex systems could be recognized on either side of the animal on the vector plots where the mean velocities were subtracted and on the vorticity plots. The vortices could be located more precisely using d. Small but significant values of the divergence in front of and

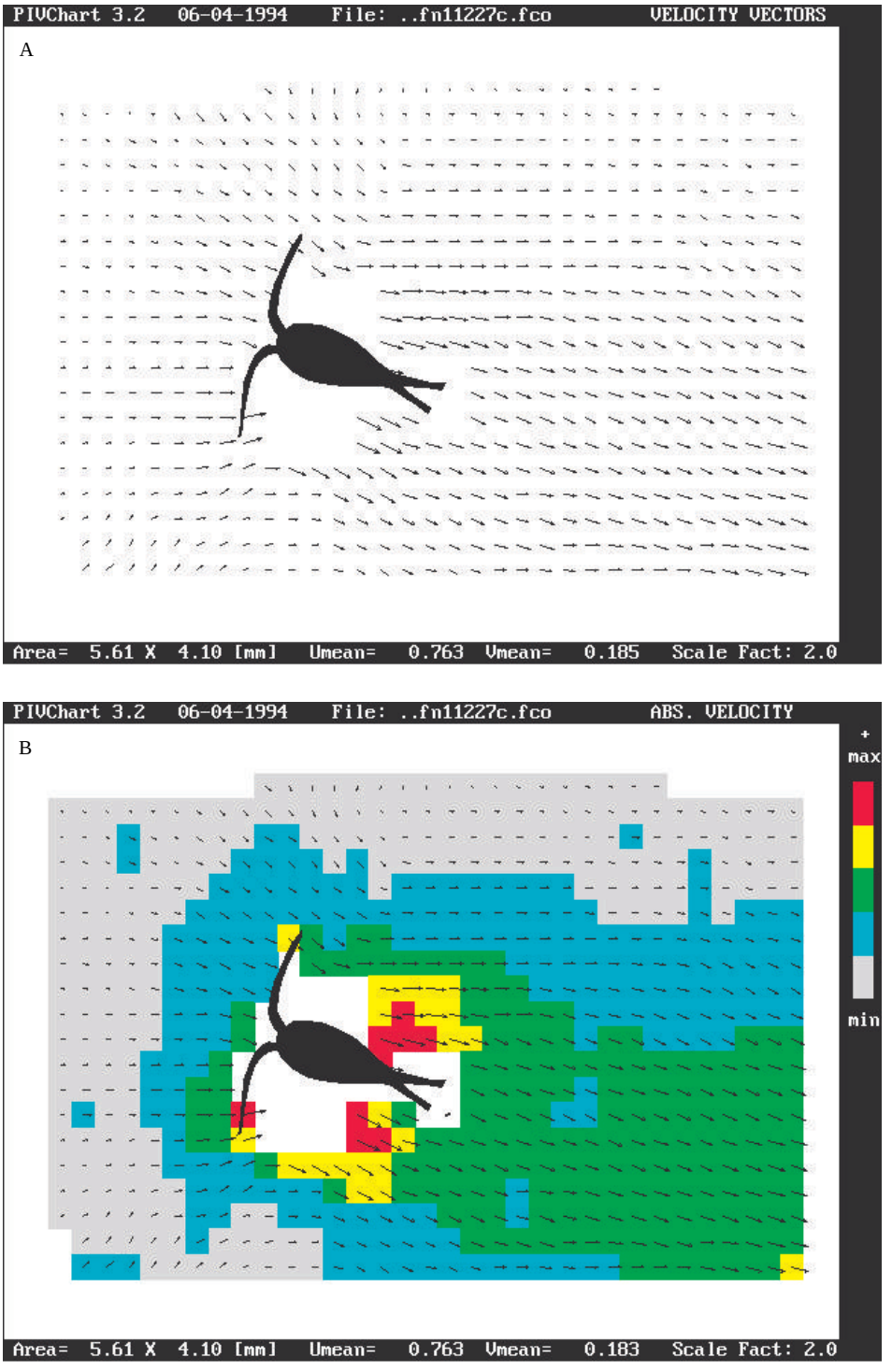

Fig. 1. (A) Flow field of one plane of the feeding current of a tethered adult copepod (*Temora longicornis*, metasome length approximately 1.0 mm), resulting from automatic analysis using SCPIV. Vectors are missing on both lateral sides of the animal because of locally high velocities and blurring by the moving swimming appendages. Vectors are scaled to a 2.0 times magnification. (B) Colour-coded diagram of the absolute velocity in the feeding current of *T. longicornis* emphasizing low flow velocities in front of the animal, high velocities near the flow-producing appendages and a large diverging and slowly decelerating jet behind the animal. Red, maximum velocity; grey, minimum velocity; vectors are scaled to a 2.0 times magnification.

behind the animal in the two-dimensional flow fields suggested a velocity component in the third dimension. This was confirmed after reconstruction of the flow in three dimensions by combining the results of flow charts of perpendicular and parallel planes. Figs 1 and 2 show an example of a flow field from the feeding current of *T. longicornis*, showing the vector flow field before and after subtracting the average velocity components (Figs 1A, 2A), as well as colour-coded diagrams of the velocity magnitude and the vorticity (Figs 1B, 2B). These results will be used to estimate the range of influence, the volume of water displaced per second and the energy dissipated by the copepod while feeding.

The ventilation current of a tube-dwelling thallassinid shrimp

The ventilation current of a tube-dwelling thallassinid shrimp (*Callianassa subterranea*, rostrum–telson length approximately 40 mm) was studied by putting the animal in a

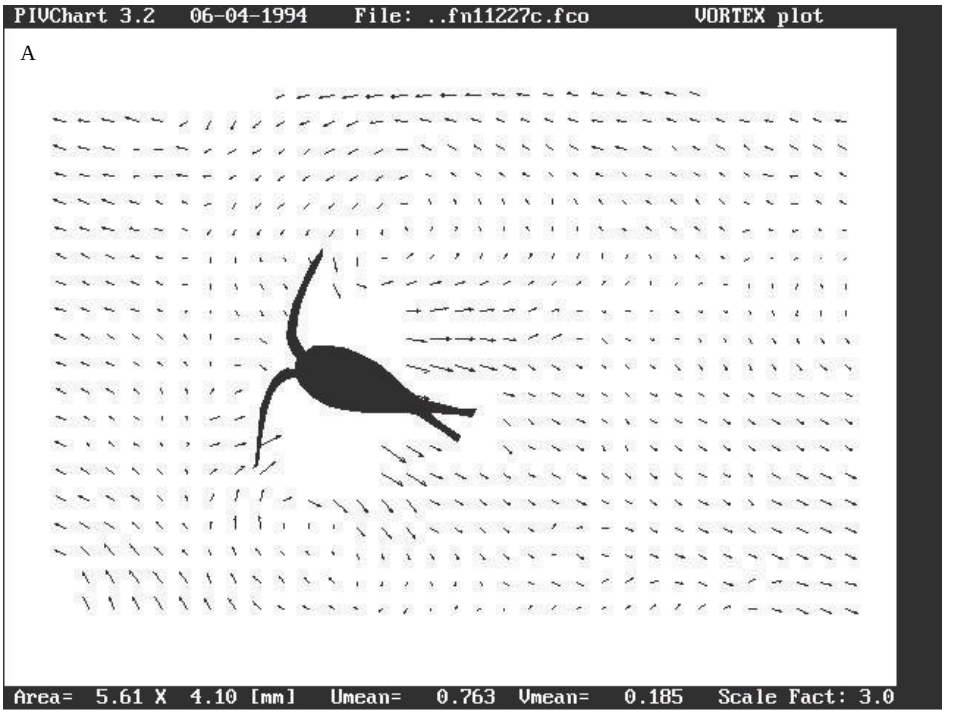

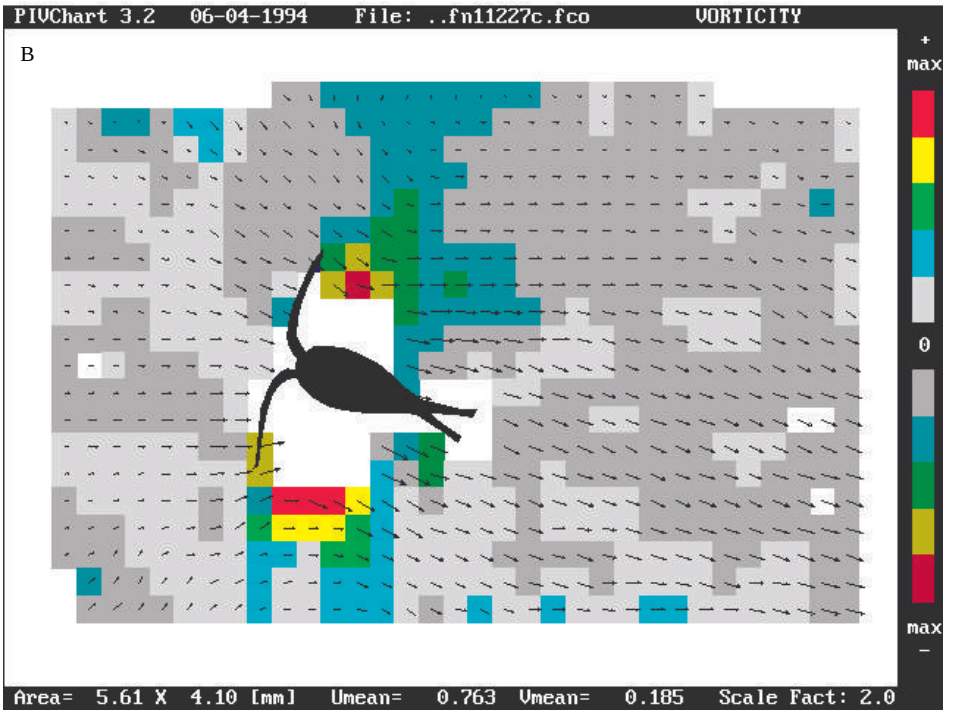

Fig. 2. (A) Velocity vectors of the flow field of the feeding current of *T. longicornis* compensated for the average flow velocities in the *x*- and *y*-directions, showing vortices symmetrically on either side of the copepod. Vectors are scaled to a 3.0 times magnification. (B) Colour-coded diagram of the vorticity in the feeding current of the copepod, showing an almost symmetrical pattern with reference to the central axis of the animal. High levels of vorticity occur on either side of the animal, showing the rotationality induced by the swimming movements. Bright colours, positive vorticity = right-turning; dark colours, negative vorticity = left-turning; red, high vorticity; grey, low vorticity.

simple artificial burrow provided with one thin-walled horizontal glass tube of 8 mm diameter. The burrow was submerged in a temperature-controlled glass aquarium containing artificial sea water. Neutrally buoyant polystyrene particles (diameter approximately 25 μm) were added to the water. The particles were illuminated using a vertical laser light sheet of about 0.5 mm thickness. The sheet crossed the central plane of the glass tube over its entire length.

The final results after processing the recordings were vector flow fields with uniformly distributed vectors, representing the spatial changes in the flow velocities. Because of the pumping of the animal, water with relatively high flow velocity entered the region behind the animal from underneath its telson. Further down the tube, the water in this jet decelerated, adopting a low Reynolds number parabolic velocity profile. The flow fields show the associated decreasing flow velocity,

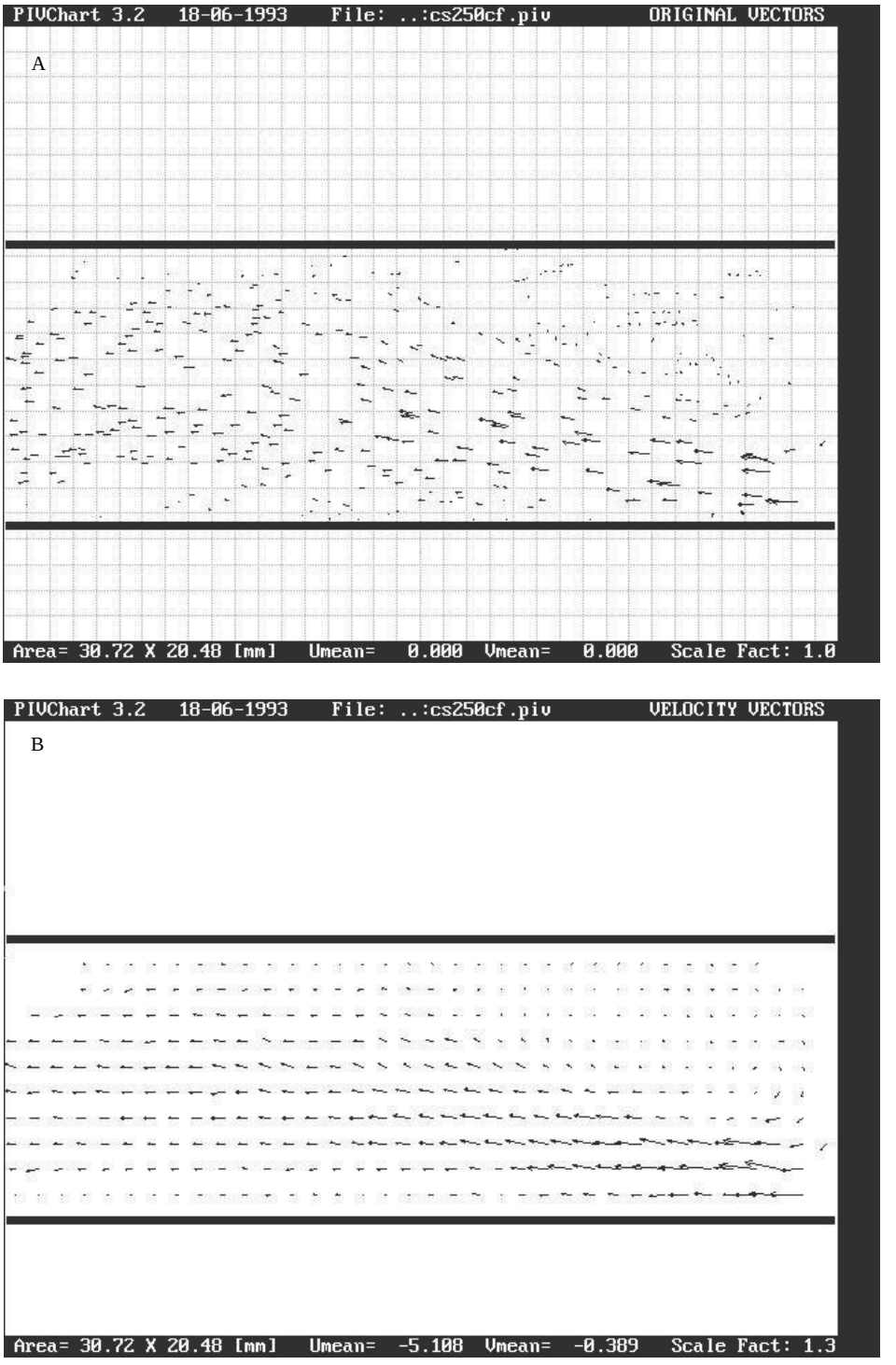

Fig. 3. (A) Velocity vectors derived directly from traced particles (PTV) in one plane of the ventilation current of a thallassinid shrimp *Callianassa subterranea* in a glass tube (rostrum–telson length approximately 40 mm, tube diameter 8 mm, wide black horizontal lines represent tube walls). The animal, situated just out of sight on the right, is ventilating by moving its three pairs of pleopods in a metachronal pattern. Particles are illuminated using a 0.5 mm laser light sheet crossing the central plane of the tube over its entire length. (B) Diagram of the velocity vector flow field reconstructed from the original particle displacement vectors as displayed in A. Velocity vectors show a much more uniform distribution and no gaps remain. Vectors are scaled to a 1.3 times magnification.

negative acceleration (a_N) and significant shear rates. A large vortex system was observed directly behind the shrimp's telson, with the velocity vectors showing rotation, high vorticity and negative *d*.

Fig. 3 shows the velocity vector flow field before (Fig. 3A) and after (Fig. 3B) processing, and Fig. 4 shows colour-coded diagrams of the velocity magnitude (Fig. 4A) and the rate of shear (Fig. 4B) directly behind an actively pumping animal. These and other results will be used to describe pleopod pumping in *Callianassa subterranea* and to validate hydrodynamical modelling on pleopod pumping in tube-living thallassinid shrimps (Stamhuis, 1991).

The vortex sheet behind a freely swimming juvenile grey mullet

The water in a 30 cm×40 cm glass aquarium containing a freely swimming juvenile grey mullet (*Chelon* sp., total length approximately 50 mm) was seeded with neutrally buoyant

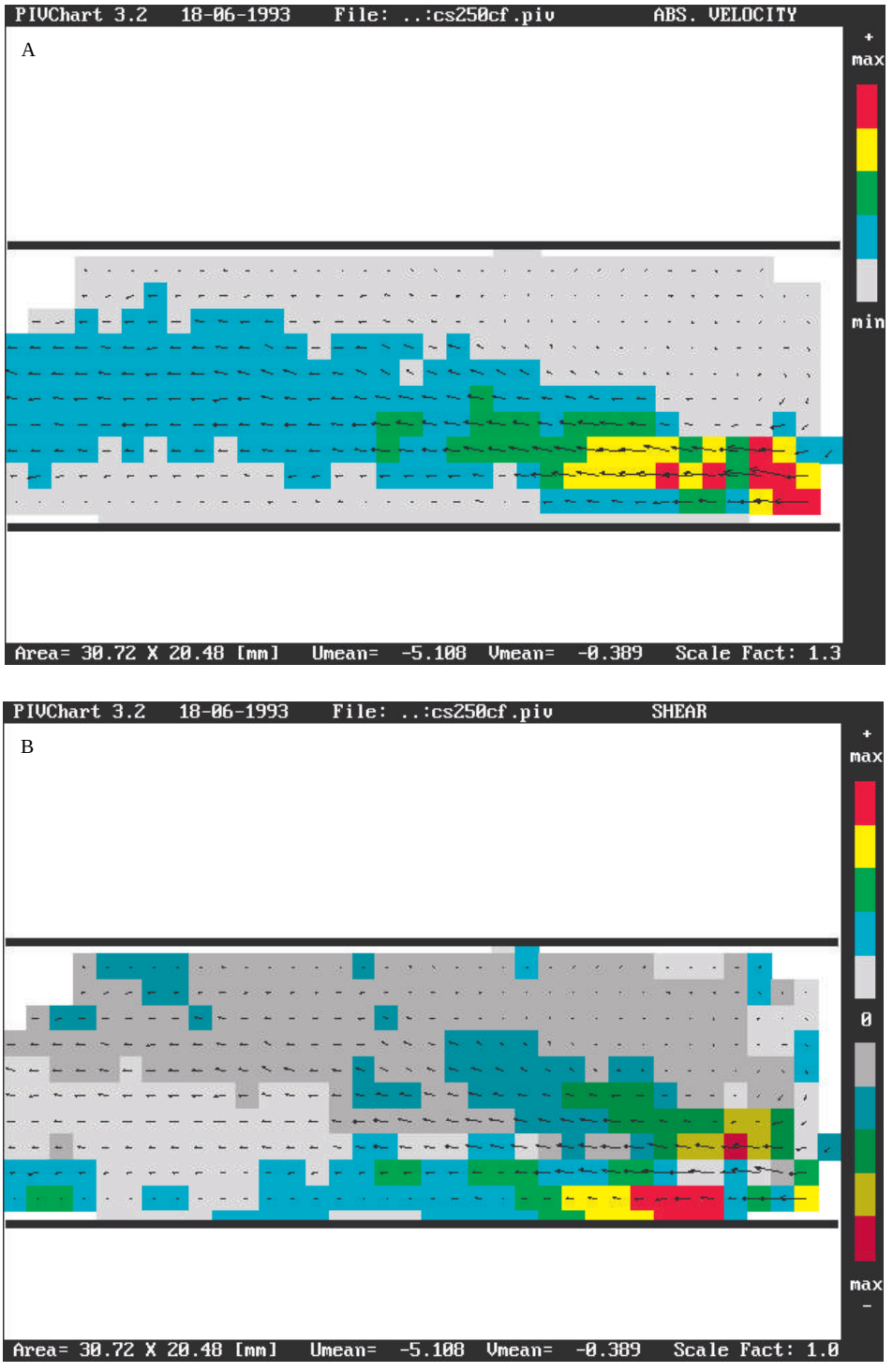

Fig. 4. (A) Colour-coded diagram of the absolute velocity in the ventilation current of *C. subterranea* in a glass tube, showing high velocities at the bottom right, where the water enters the area just behind the animal from underneath its telson in a sharply defined jet, and then decelerates when diverging over the whole diameter of the tube. Wide black horizontal lines represent tube walls, red, maximum velocity; grey, minimum velocity. (B) Colour-coded diagram of the rate of shear in the ventilation current of *C. subterranea* just behind the animal. The high-velocity jet coming from underneath the animal's telson is decelerated and diverges over the whole tube owing to the high rates of shear caused by viscous friction. High rates of shear and relatively large iso-shear areas occur at the lower tube wall near the jet. Shallower shear gradients are visible in the upper part and just above the jet, interacting with a large slowly circulating vortex system behind the animal's telson, above the jet. Bright colours, positive shear = gradient to the left; dark colours, negative shear = gradient to the right; red, high rate of shear; grey, low rate of shear.

white Pliolite particles (BASF, diameter approximately 50 μm) and was illuminated with a horizontal laser light sheet of 0.3–0.5 mm thickness. Sequences of video images, recorded from above, were analyzed to make vector maps of the vortex street left behind by the swimming fish.

A vector flow field resulting from the SCPIV analysis of two successive video images after the fish had passed from left to right in the upper part of the image showed velocity vectors with a rather obscure geometry (Fig. 5A, vectors). Neither well-developed vortices nor a vortex street could be recognized easily. The discriminant for complex eigenvalues *d*, however, indicated an array of vortices along the path where the fish had passed (Fig. 5A, colour coding). These vortices were emphasized by subtracting the average velocities in the *x*- and *y*-directions (Fig. 5B), as shown in, for example, the dark square around a *d* peak in Fig. 5A compared with a clear vortex in the same square in Fig. 5B. The net result is a clearer picture of the vortex street, consisting of vortices distributed along the

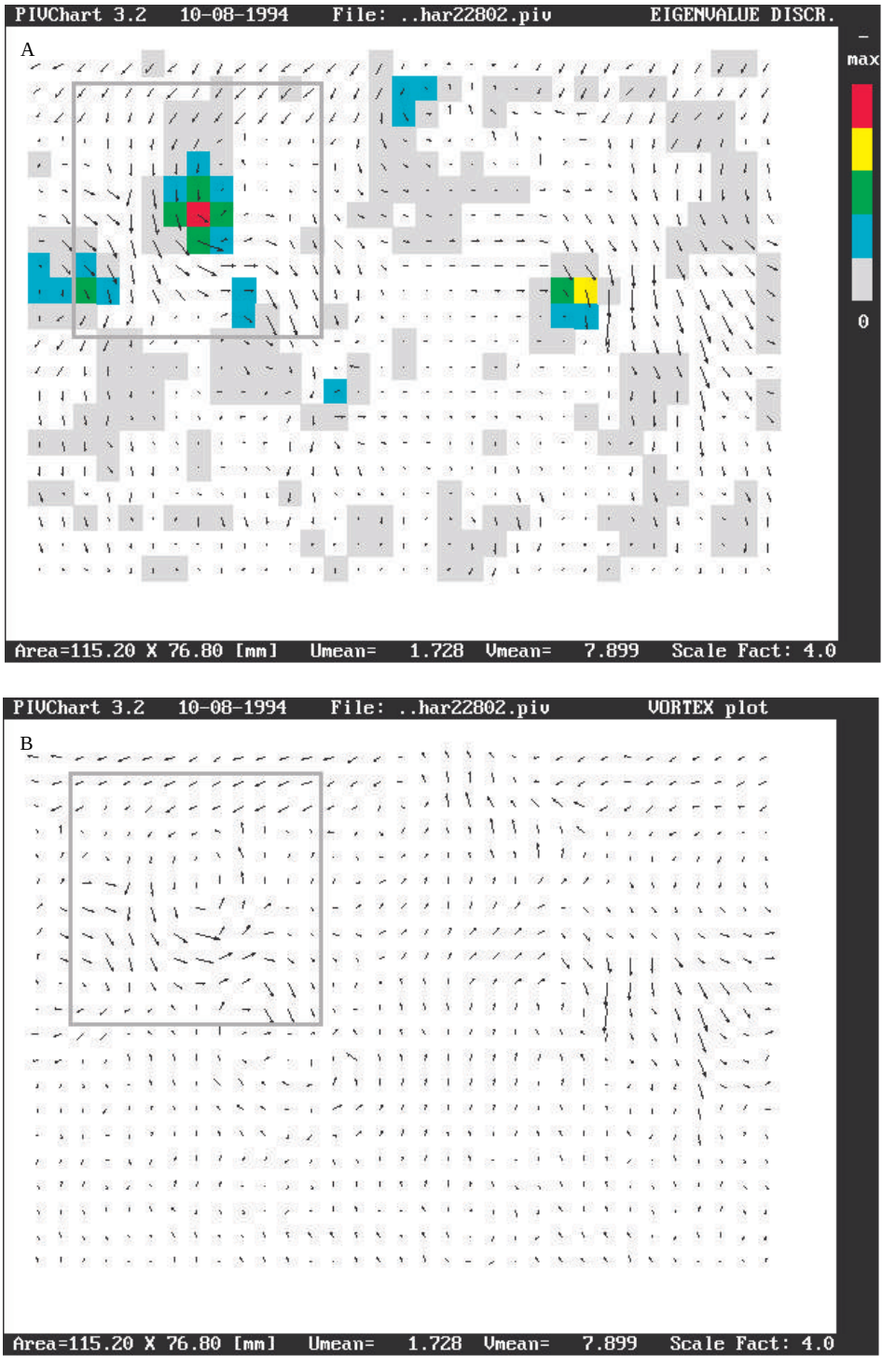

Fig. 5. (A) Vector flow field of the swimming path (in top view) of a 5 cm long grey mullet (*Chelon* sp.) which passed in the upper half of the diagram from left to right, resulting from automatic analysis using SCPIV. Although vortices are barely recognizable by eye, the discriminant for complex eigenvalues *d*, displayed in relative colour coding, indicates their presence and location. Vectors are scaled to a 4.0 times magnification; red, maximum negative *d*; grey, minimum negative *d*. (B) Flow velocity vectors of the grey mullet swimming path, compensated for the average flow velocities in the *x*- and *y*-directions, showing alternating vortices on either side of the track as well as axially and laterally directed jets. The square emphasizes an example of a well-developed vortex in the area around a *d* peak in A, where a vortex was hardly visible before compensation. The flow field is somewhat disturbed by background flow due to earlier passes of the fish. Vectors are scaled to a 4.0 times magnification.

swimming path of the fish (Fig. 5B). The pattern in Fig. 5B is somewhat disturbed by background flow remaining from earlier passes of the fish.

Results such as these will be used to study and describe vortex formation and vortex morphology of swimming larval and juvenile fish in relation to flow regime and Reynolds number and to estimate the energetic costs of swimming using momentum and vortex ring models.

Discussion

The two PIV techniques presented have their specific advantages and disadvantages. SCPIV offers high accuracy combined with the convenience of automatic image processing, but is more critical on image quality and maximum particle displacement in relation to sub-image size. PTV does not need high seeding densities (probably disturbing an animal's behaviour) and allows relatively large particle

displacements, but the manual processing is quite laborious. When applied in the right situation, both methods yield accurate quantitative velocity information that allows extensive post-processing analysis. In some cases, a combination of the two methods might yield the best results: SCPIV can be used to analyse parts of the images with small particle displacements and shallow gradients, while areas with large particle displacements can be analyzed using PTV.

The results of our flow analysis can be used to calculate dissipated energy from viscous deformation (Yen *et al.* 1991), acceleration rates or momentum in a wake. Insight into the energetic consequences for animals of moving (in) fluid can also be gained in combination with vortex theories (Rayner, 1979*a*,*b*,*c*; Spedding *et al.* 1984; Spedding, 1986, 1987*a*,*b*). The data processing and the presentation of the results offer the opportunity to compare particle paths, resultant velocity vectors or dissipated energy with theoretical predictions from numerical simulations using simple hydrodynamic modelling or computational fluid dynamics based on the Navier–Stokes equations (Roache, 1982; Imaichi and Ohmi, 1983). The versatile character of the technique makes it applicable to a wide range of fluid mechanical subjects within biological research.

We would like to thank Ms Luca A. van Duren for permission to use her results in application number 1 and Ms Ulrike Müller for her cooperation in studying the vortex street of a swimming fish, as described in application number 3. We are grateful to Drs G. R. Spedding and J. L. van Leeuwen for their comments, which encouraged and stimulated us to improve the paper, in particular the error evaluation. Finally, we would like to thank Dr W. Ravenek of the Free University of Amsterdam for improving the performance of the convolution routine.

References

ADRIAN, R. J. (1991). Particle imaging techniques for experimental fluid mechanics. *A. Rev. Fluid Mech.* **23**, 261–304.

AGÜI, J. C. AND JIMÉNEZ, J. (1987). On the performance of particle tracking. *J. Fluid Mech.* **185**, 447–468.

BARLOW, D., SLEIGH, M. A. AND WHITE, R. J. (1993). Water flows around the comb plates of the ctenophore *Pleurobrachia* plotted by computer: a model system for studying propulsion by antiplectic metachronism. *J. exp. Biol.* **177**, 113–128.

CRAIG, D. A. AND CHANCE, M. M. (1982). Filterfeeding in larvae of *Similiidae* (Diptera: Culicomorpha): Aspects of functional morphology and hydrodynamics. *Can. J. Zool.* **60**, 712–724.

DROST, M. R., OSSE, J. W. M. AND MULLER, M. (1988). Prey capture by fish larvae, water flow patterns and the effect of escape movements of prey. *Neth. J. Zool.* **38**, 23–45.

EMLET, R. B. (1990). Flow fields around ciliated larvae: effects of natural and artificial tethers. *Mar. Ecol. Progr. Ser.* **63**, 211–225.

FENCHEL, T. (1980). Relation between particle size selection and clearance in suspension feeding ciliates. *Limnol. Oceanogr.* **25**, 733–738.

FIELDS, D. AND YEN, J. (1993). Outer limits and inner structure: The 3-dimensional flow field of *Pleuromamma xiphias* (Calanoida: Metridinidae). *Bull. mar. Sci.* **53**, 84–95.

GALLAGER, S. M. (1993). Hydrodynamic disturbances produced by small zooplankton: case study for veliger larva of a bivalve mollusc. *J. Plankton Res.* **15**, 1277–1296.

GILMOUR, T. H. J. (1986). Streamlines of particle paths in the feeding mechanisms of larvae of the sea urchin *Lytechinus pictus* Verrill. *J. exp. mar. Biol. Ecol.* **95**, 27–36.

GONZALES, R. AND WINTZ, P. (1987). *Digital Image Processing.* Reading, MA: Addison-Wesley Publishing Co.

GREVILLE, T. N. E. (1969). *Theory and Applications of Spline Functions.* New York: Academic Press.

GUPTA, A. K. AND LILLEY, D. G. (1985). *Flowfield Modelling and Diagnostics.* Tunbridge Wells, UK: Abacus Press.

HESSELINK, L. (1988). Digital image processing in flow visualization. *A. Rev. Fluid Mech.* **20**, 421–485.

HINSCH, K. D. (1993). Particle image velocimetry. In *Speckle Metrology* (ed. R. S. Sirohi), pp. 235–324. New York: Marcel Dekker Inc.

IMAICHI, K. AND OHMI, K. (1983). Numerical processing of flow visualization pictures: measurement of two-dimensional vortex flow. *J. Fluid Mech.* **129**, 283–311.

JØRGENSEN, C. B. (1982). Fluid mechanics of the mussel gill: the lateral cilia. *Mar. Biol.* **70**, 275–281.

KOEHL, M. A. R. AND STRICKLER, J. R. (1981). Copepods feeding current: Food capture at low Reynolds number. *Limnol. Oceanogr.* **26**, 1062–1073.

LABARBERA, M. (1981). Water flow patterns in and around three species of articulate brachiopods. *J. exp. mar. Biol. Ecol.* **55**, 185–206.

LIGHTHILL, J. (1986). *An Informal Introduction to Theoretical Fluid Mechanics.* Oxford: Oxford University Press.

LOURENÇO, L. M. (1991). Particle image velocimetry: photographic and video techniques. In *Laser Velocimetry.* Brussels: Von Karman Institute for Fluid Dynamics. Lecture Series 1991-05.

MARRASÉ, C., COSTELLO, J. H., GRANATA, T. AND STRICKLER, J. R. (1990). Grazing in a turbulent environment: Energy dissipation, encounter rates and efficacy of feeding in *Centropagus hamatus*. *Proc. natn. Acad. Sci. U.S.A.* **87**, 1653–1657.

MERZKIRCH, W. (1974). *Flow Visualisation.* New York: Academic Press.

OKUBO, A. AND EBBESMEYER, C. C. (1976). Determination of vorticity, divergence and deformation rates from analysis of drogue observations. *Deep-Sea Res.* **23**, 349–352.

PAFFENHÖFER, G. A., STRICKLER, J. R. AND ALCARAZ, M. (1982). Suspension-feeding by herbivorous calanoid copepods: a cinematographic study. *Mar. Biol.* **67**, 193–199.

RAFFEL, M., LEITL, B. AND KOMPENHANS, J. (1992). Data validation for particle image velocimetry. In *Laser Techniques and Applications in Fluid Mechanics* (ed. R. J. Adrian, D. F. G. Durao, F. Durst, M. M. Heitor, M. Marda and J. H. Whitelaw). Sixth International Symposium, Lisbon, Portugal, 1992. Berlin: Springer Verlag.

RAYNER, J. M. V. (1979*a*). A new approach to animal flight mechanics. *J. exp. Biol.* **80**, 17–54.

RAYNER, J. M. V. (1979*b*). A vortex theory of animal flight. I. The vortex wake of a hovering animal. *J. Fluid Mech.* **91**, 697–730.

RAYNER, J. M. V. (1979*c*). A vortex theory of animal flight. II. The forward flight of birds. *J. Fluid Mech.* **91**, 731–763.

ROACHE, P. J. (1982). *Computational Fluid Dynamics*. Albuquerque: Hermosa Publishers.

SPEDDING, G. R. (1986). The wake of a jackdaw (*Corvus monedula*) in slow flight. *J. exp. Biol.* **125**, 287–307.

SPEDDING, G. R. (1987*a*). The wake of a kestrel (*Falco tinnunculus*) in gliding flight. *J. exp. Biol*. **127**, 45–57.

SPEDDING, G. R. (1987*b*). The wake of a kestrel (*Falco tinnunculus*) in flapping flight. *J. exp. Biol.* **127**, 59–78.

SPEDDING, G. R., RAYNER, J. M. V. AND PENNYCUICK, C. J. (1984). Momentum and energy in the wake of a pigeon (*Columba livia*) in slow flight. *J. exp. Biol.* **111**, 81–102.

SPEDDING, G. R. AND RIGNOT, E. J. M. (1993). Performance analysis and application of grid interpolation techniques for fluid flows. *Exp. Fluids* **15**, 417–430.

SPONAUGLE, S. (1991). Flow patterns and velocities around a suspension-feeding gorgonian polyp: evidence from physical models. *J. exp. mar. Biol. Ecol.* **148**, 135–145.

STAMHUIS, E. J. (1991). Pleopod movements of a tube-dwelling decapod. *J. mar. biol. Ass. U.K.* **71**, 722

STRATHMANN, R. R. (1971). The feeding behavior of planktotrophic echinoderm larvae: mechanisms, regulation and rates of suspension-feeding. *J. exp. mar. Biol. Ecol.* **6**, 109–160.

STRATHMANN, R. (1973). Function of lateral cilia in suspension feeding of lophophorates (Brachiopoda, Phoronida, Ectoprocta). *Mar. Biol.* **23**, 129–136.

STRICKLER, J. R. (1982). Calanoid copepods, feeding currents and the role of gravity. *Science* **218**, 158–160.

STRICKLER, J. R. (1985). Feeding currents in calanoid copepods: two new hypotheses. In *Physiological Adaptations of Marine Animals*, vol. 39 (ed. M. S. Laverack), pp. 459–485. *Symp. Soc. exp. Biol*.

VAN LEEUWEN, J. L. (1984). A quantitative study of flow in prey capture by Rainbow Trout *Salmo gairdneri*, with general consideration of the actinopterygian feeding mechanism. *Trans. zool. Soc. Lond.* **37**, 171–227.

VOGEL, S. (1981). *Life in Moving Fuids.* Boston: Willard Grant Press.

VOLLMERS, H., KREPLIN, H.-P. AND MEIER, H. U. (1983). Separation and vortical-type flow around a prolate spheroid – evaluation of relevant parameters. *NATO AGARD Conference Proceedings No.* **342**, pp. 14/1–14/14.

WILLERT, C. E. AND GHARIB, M. (1991). Digital particle image velocimetry. *Exp. Fluids* **10**, 181–193.

YEN, J., SANDERSON, B., STRICKLER, J. R. AND OKUBO, A. (1991). Feeding currents and energy dissipation by *Euchaeta rimana*, a subtropical pelagic copepod. *Limnol. Oceanogr.* **36**, 362–369.